

Banner appropriate to article type will appear here in typeset article

Progressive Mixture-of-Experts with autoencoder routing for continual RANS turbulence modelling

Haoyu Ji^{1,2}, Yinhang Luo¹, Hanyu Zhou^{1,2} and Yaomin Zhao^{1,2}

¹HEDPS, Center for Applied Physics and Technology, School of Mechanics and Engineering Science, Peking University, Beijing 100871, China

²State Key Laboratory for Turbulence and Complex Systems, School of Mechanics and Engineering Science, Peking University, Beijing 100871, China

Corresponding author: Yaomin Zhao, yaomin.zhao@pku.edu.cn

(Received xx; revised xx; accepted xx)

Developing Reynolds-averaged Navier–Stokes (RANS) turbulence models that remain accurate across diverse flow regimes remains a long-standing challenge. In this work, we propose a novel framework, termed the progressive mixture-of-experts (PMoE), designed to enable continual learning for RANS turbulence modelling. The framework employs a modular autoencoder-based router to associate each flow scenario with a specialised turbulence model, referred to as an expert. When an unseen flow regime cannot be adequately represented by the existing router and expert set, a new expert together with its routing component can be introduced at low cost, without modifying or degrading previously trained ones, thereby naturally avoiding catastrophic forgetting. The framework is applied to a range of flows with distinct physical characteristics, including baseline airfoil wakes, wall-attached flows, separated flows and corner-induced secondary flows. The resulting PMoE model effectively integrates multiple experts and achieves improved predictive accuracy across both seen and unseen test cases. Owing to sparse activation, model expansion does not incur additional computational cost during inference. The proposed framework therefore provides a scalable pathway towards lifelong-learning turbulence models for industrial computational fluid dynamics.

Key words: machine learning, turbulence modelling

1. Introduction

Reynolds-averaged Navier-Stokes (RANS), supported by turbulence closure models, remains a predominant computational fluid dynamics (CFD) approach in industry. RANS maintains a balance between computational efficiency and accuracy for predicting mean flow quantities, making it critical for applications across aerospace, automotive, and energy sectors (Rumsey 2014; Bush *et al.* 2019). The main difficulty, however, lies in closing the

Reynolds stress tensor, especially for complex flows such as boundary layer transition and separation. Traditional closures are based on physical arguments, empirical tuning, or, more recently, data-driven calibration (Lauder & Sharma 1974; Spalart & Allmaras 1992; Wilcox 2008; Ling *et al.* 2016).

The demand for improving turbulence models has led to the use of machine learning methods (Duraisamy *et al.* 2019; Brunton *et al.* 2020). Many machine learning methods have been introduced into turbulence modeling, including Bayesian optimization (Xiao *et al.* 2016), ensemble Kalman filter (Zhang *et al.* 2022), adaboost decision trees (Ling & Templeton 2015), random forests (Wang *et al.* 2017), tensor basis neural networks (Ling *et al.* 2016), symbolic regression (SR) (Weatheritt & Sandberg 2016; Zhao *et al.* 2020; Schmelzer *et al.* 2020), among others. In these studies, the modeling strategies vary considerably, from correcting the parameters of linear eddy viscosity models to forming completely new nonlinear eddy viscosity models, with the optimizing targets vary from predicting transition (Duraisamy *et al.* 2015; Zhang *et al.* 2023) to characterizing boundary layer separation (Zhu *et al.* 2019; Wu & Zhang 2023). These models, which are typically trained to improve predictive accuracy for specific cases, can thus be termed as expert models.

Despite considerable advances, achieving robust generalization for data-driven turbulence models remains not only an active research area but also a significant challenge. Based on the accumulated experience from industrial turbulence simulations, evidence suggests that a universal, simple, and local turbulence model may be difficult to achieve (Rumsey & Coleman 2022). To enhance generalization for traditional turbulence models, one approach is to perform parameter calibration in various application scenarios. The GEKO model, for example, provides empirical parameter combination for the $k - \omega$ model under a wide range of cases (Menter & Matyushenko 2025). This cross-case generalization capability, *i.e.* the capability to make accurate predictions in diverse flow scenarios, is particularly important and even more challenging for models trained by machine learning methods (Sandberg & Zhao 2022).

To achieve generalization across diverse flow scenarios, researchers have explored numerous approaches that leverage model architecture design, training data diversity, feature engineering, and physical constraints. These efforts can be broadly categorized into three distinct paradigms. The first strategy focuses on parameter calibration using data-driven approaches to enhance adaptability. For instance, Bin *et al.* (2023) constructed a unified model by fine-tuning the parameters of the Spalart-Allmaras (SA) model, thereby extending its applicability across various flows. The second approach seeks to improve generalization through multi-case training strategies, where the model is exposed to distinct geometries and physical characteristics during the learning phase. Notable examples include the symbolic-regression-based training developed by Fang *et al.* (2023) and the multi-case surrogate optimization by Amarloo *et al.* (2023). The third category involves model mixing or ensemble methods, which utilize machine-learning-based weighting functions to blend multiple baseline models. In a series of recent studies (de Zordo-Banliat *et al.* 2024; Cherroud *et al.* 2025; Oulghelou *et al.* 2025), machine learning methods were employed to train weighting functions, successfully leveraging the strengths of different data-driven models to achieve improved accuracy across multiple cases. Parallel to these RANS-based developments, significant progress has also been made in wall-modeled large eddy simulations (WMLES) (Lozano-Durán & Bae 2023; Arranz *et al.* 2024), in which model trained on several canonical flows exhibits good agreement with reference data for both canonical tests and realistic aircraft configurations.

It should be noted that most existing data-driven models are considered reliable only within the vicinity of their training distributions, while applying to completely unknown

flow regimes remains a critical challenge. In practical CFD applications, users are frequently confronted with novel flow configurations and operating conditions distinct from prior experiences. Directly training the existing model with newly obtained data often degrades its original performance, which is known as catastrophic forgetting (French 1999). Although a common approach is to retrain the model on both pre-existing and new data, it often comes with a high computational cost. In order to achieve continual learning for WMLES, Zhang *et al.* (2025) proposed a additive framework for training wall models, showing promising success in a series of cases. Nevertheless, novel frameworks with the capability of continual learning are still needed for developing generalizable RANS models.

To achieve a framework capable of sustainable generalization, we propose a novel approach termed progressive mixture-of-experts (PMoE) in the present study. The PMoE method is founded on the mixture-of-experts (MoE) architecture (Jacobs *et al.* 1991), which has been the subject of much research in the field of machine learning (Shazeer *et al.* 2017; Fedus *et al.* 2022) and becomes very popular in the field of large language models due to its scalability (Du *et al.* 2022; Dai *et al.* 2024). Building on the typical architecture consisting of a router and a group of experts, the MoE offers a distinct advantage for turbulence modelling, *i.e.* the decomposition of a complex, high-dimensional physical problem into manageable sub-tasks. Central to this architecture is the mechanism of sparse activation. Unlike monolithic models, the router in an MoE network activates only a specific subset of expert models for a given local flow state, leaving the majority silent during the inference process. This property is crucial for industrial CFD applications, as it does not incur the prohibitive computational cost usually associated with large-scale neural networks, while achieving sufficient representational expressiveness in order to deal with various scenarios featuring different flow physics.

One important novel feature of the present PMoE framework, which is missing for the generic MoE structure, is the continual-learning capability. This is in order to achieve sustainable generalization, enabling the model to incorporate newly introduced datasets without full retraining. Accordingly, the PMoE is designed to be equipped with a modular autoencoder-based router. The PMoE framework is applied to develop a turbulence model by successively introducing the data of four flow regimes, including baseline airfoil wake, wall-attached flow, separated flow and corner-induced secondary flow. The trained PMoE model is then extensively assessed both *a priori* and *a posteriori*, validating its performance on both in-distribution and out-of-distribution datasets. The objective is mainly to show the ability of PMoE to incorporate new flow scenarios without retraining or degrading existing experts.

Before introducing the framework in detail, it is important to highlight three key issues that need to be addressed to develop a PMoE turbulence model generalizable for various flow regimes. First, the PMoE framework needs to classify diverse flow scenarios in an unsupervised manner using only RANS data, and this requirement bring a significant challenge regarding the selection and extraction of appropriate physical features for the pre-processing procedure to serve as effective model inputs. Second, the router architecture must support continual-learning capabilities, determining whether a new case belongs to a known flow regime or represents a novel one. For the latter, the architecture must allow for the rapid addition of new modules without the need for retraining. Finally, the distinct nature of turbulence across different flows implies that a unified model form may be insufficient (Duraisamy *et al.* 2019), and different flow regimes often require fundamentally different correction forms. Consequently, the design of specific expert architectures tailored to these varying physical characteristics is crucial for the success of a truly generalizable model. These topics will be addressed in detail in the following sections.

This paper is organized as follows. The structure of the new framework is discussed in § 2. The training process and the setting of cases are introduced in § 3. The model assessment, validation and computational cost analysis are given in § 4. Finally, conclusions are offered in § 5.

2. Methodology

The MoE framework, which has the potential to develop generalizable turbulence models, is introduced in § 2.1. Moreover, the router part of a generic MoE framework is typically implemented by multilayer perceptron (MLP), which enables multi-task learning but requires further improvement for continual learning. In § 2.2, we introduce the PMoE structure, demonstrating how the newly proposed framework facilitates continual generalization of turbulence modelling.

2.1. Introduction to the generic mixture-of-experts framework

As shown in figure 1, the generic MoE consists of a set of n experts $\{E_1, \dots, E_n\}$ and a gating network (also named as a router) G , and the key advantage of this framework is the decomposition of a complex, high-dimensional problem into manageable sub-tasks dealt by different experts. For turbulence modelling, each expert E_i can be viewed as a specialized closure model tailored for a specific flow regime, while the router G functions as a flow regime classifier.

For a set of n experts, the output \mathbf{y} for a given input flow state \mathbf{x} is the weighted sum of expert predictions:

$$\mathbf{y} = \sum_{i=1}^n G(\mathbf{x})_i E_i(\mathbf{x}). \quad (2.1)$$

Here, $G(\mathbf{x})_i$ is the i^{th} component of the output vector of G and represents the probability (or confidence) that the corresponding flow \mathbf{x} belongs to the regime governed by expert i . A simple choice of the gating function (Jordan & Jacobs 1994), as shown in figure 1(b) for example, is to multiply the input \mathbf{x} by a trainable weighting matrix \mathbf{W}_g and then apply the $\text{Softmax}(\cdot)$ function, as

$$G_\sigma(\mathbf{x}) = \text{Softmax}(\mathbf{x} \mathbf{W}_g), \quad (2.2)$$

where the subscript σ denotes the Softmax nonlinearity.

The key advantage of the MoE framework lies in its sparse activation mechanism, which dramatically reduces computational costs while maintaining model capacity. Typically, sparse MoE employs a top- k routing strategy where only the most relevant k experts are activated for each input. For example, we set $k = 1$ in our current implementation, thus the router selects the one most relevant expert per input token, ensuring that the rest $n - 1$ experts remain completely dormant during model inference. With this feature of sparse activation, the computational cost of the MoE model, despite having a large pool of experts $\{E_1, \dots, E_n\}$, scales only with the size of a single expert rather than the entire ensemble. Consequently, the inference cost remains nearly constant regardless of the total number of experts, enabling the deployment of extremely large-scale models with billions or even trillions of parameters with relatively low computational requirements (Shazeer *et al.* 2017; Fedus *et al.* 2022).

While the generic MoE offers a path toward modular turbulence modelling, applying it to industrial CFD requires a capability that standard architectures lack, *i.e.* continual learning. A truly generalizable turbulence model must be able to assimilate new flow physics (e.g., transitioning from simple shear flows to complex corner separations) without

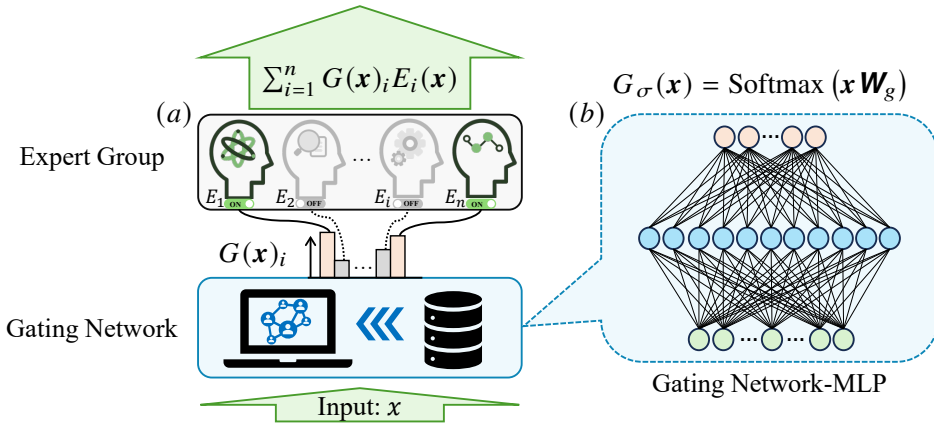


Figure 1. Schematic of the generic MoE framework with a MLP softmax gating network. (a) The whole process of the MoE framework. (b) Zoom-in view of a gating network based on MLP.

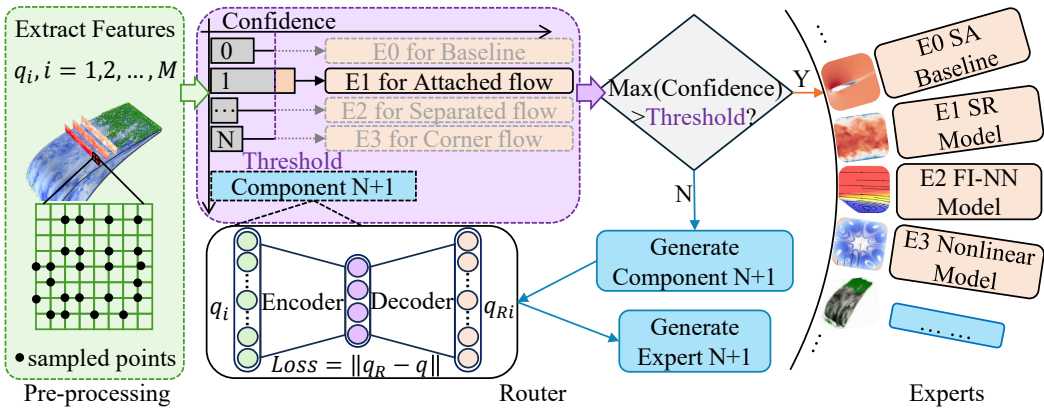


Figure 2. Schematic of the proposed PMoE framework.

“forgetting” previously learned regimes. However, standard MLP-based routers in figure 1 are highly susceptible to catastrophic forgetting (French 1999), as updating the weights to accommodate a new flow regime often degrades the classification accuracy for existing ones.

2.2. Progressive mixture-of-experts framework for turbulence modelling

In the present study, we propose the PMoE framework for data-driven turbulence modelling with the ability of continual learning. As shown by the schematic in figure 2, the PMoE framework consists of three key components, including the procedure of pre-processing to extract flow features as model inputs, the router structure responsible for classifying various types of flows, and a group of experts each trained for a specified flow scenario. In particular, the PMoE replaces the MLP router with a modular bank of autoencoders, each dedicated to recognizing a specific flow signature. This ensures that the introduction of a new expert and its corresponding router module does not interfere with the existing modules. Accordingly, the PMoE framework is expected to develop progressively with new datasets introduced successively, and the details are discussed in the following.

Feature (q_i)	Description	Raw feature (\hat{q}_i)	Normalization factor (q_i^*)
q_1	Vorticity magnitude	$\ \mathbf{W}\ $	$\ \mathbf{S}\ $
q_2	Ratio of excess rotation rate to strain rate (Q criterion)	$\frac{1}{2}(\ \mathbf{W}\ ^2 - \ \mathbf{S}\ ^2)$	$\ \mathbf{S}\ ^2$
q_3	Cratio of pressure normal stresses to shear stresses	$\sqrt{\frac{\partial \mathbf{P}}{\partial x_i} \frac{\partial \mathbf{P}}{\partial x_i}}$	$\frac{1}{2}\rho \frac{\partial U_k^2}{\partial x_k}$
q_4	Distance to the nearest wall	d	L_{ref}
q_5	SA viscosity	$\tilde{\nu}$	100ν
q_6	Pressure gradient along streamline	$U_l \frac{\partial \mathbf{P}}{\partial x_l}$	$\sqrt{\frac{\partial \mathbf{P}}{\partial x_j} \frac{\partial \mathbf{P}}{\partial x_j} U_i U_i}$
q_7	Nonorthogonality between velocity and its gradient (Gorle <i>et al.</i> 2012)	$\left U_i U_j \frac{\partial U_i}{\partial x_j} \right $	$\sqrt{U_l U_l U_i \frac{\partial U_i}{\partial x_j} U_k \frac{\partial U_k}{\partial x_j}}$

Table 1. Flow features used as input in the framework. \mathbf{W} is the rotation rate tensor, \mathbf{S} is the strain rate tensor, ρ is the fluid density, ν is the fluid viscosity, $\tilde{\nu}$ is the SA modified turbulent eddy viscosity, d is the distance to the nearest wall, L_{ref} is the reference height, and U_i is the mean velocity. The normalized feature q_i is obtained by normalizing the corresponding raw features value \hat{q}_i with normalization factor q_i^* according to $q_i = \hat{q}_i / (|\hat{q}_i| + |q_i^*|)$.

2.2.1. Feature extraction and physics-informed sampling

During the pre-processing stage, the input to the PMoE framework relies on local flow features extracted from a baseline RANS calculation. In the present study, we use the SA model (Spalart & Allmaras 1992) as the baseline due to its wide applications. Following previous data-driven RANS efforts (Ling & Templeton 2015; Wang *et al.* 2017), we construct an input vector $\mathbf{x} = [q_1, q_2, \dots, q_M]$ consisting of $M = 7$ flow features, as detailed in table 1. Note that the listed variables are normalized in a way of $A/(|A| + |B|)$ to ensure consistent scaling across different flow regimes.

We note that the features listed in Table 1 are not universally effective across all flow regimes. Prior studies (Yin *et al.* 2020; de Zordo-Banliat *et al.* 2024; Cherroud *et al.* 2025) suggest that a subset of these variables may often be sufficient for specific cases, and methods such as permutation feature importance (PFI) (Wu *et al.* 2025) can be employed to identify the relevant features for a specific case. Nevertheless, to accommodate future applications that may involve a broad range of flow regimes with distinct critical features, we adopt the full set as the model input.

A critical challenge in training a generalizable router is ensuring that the training data represents the dynamically active regions of the flow, rather than being dominated by the free stream or quiescent zones. Therefore, we employ a physics-informed sampling strategy during the pre-processing stage. Rather than uniformly sampling the entire computational domain, the sampling region is restricted based on the underlying flow physics. Grid points are selected only where either the strain-rate magnitude $\|\mathbf{S}\|$ or the vorticity magnitude $\|\mathbf{W}\|$ exceeds a specific threshold relative to the domain statistics. Specifically, we define

the sampling mask \mathcal{M} such that a point is included if

$$\|\mathbf{W}_j\| > \epsilon \cdot \text{median}(\|\mathbf{W}\|) \quad \text{or} \quad \|\mathbf{S}_j\| > \epsilon \cdot \text{median}(\|\mathbf{S}\|), \quad (2.3)$$

where $\|\mathbf{W}_j\|$ and $\|\mathbf{S}_j\|$ denotes the magnitudes of vorticity and strain-rate at the j^{th} sampled point, respectively, and ϵ is a thresholding parameter set to 0.05 in the present study. This criterion ensures that the selected samples are concentrated in boundary layers, shear layers, and separation zones, effectively filtering out grid points of limited physical significance. From this masked region, N points are randomly sampled to form the input matrix $\mathbf{X} \in \mathbb{R}^{N \times M}$.

2.2.2. Modular autoencoder-based router for continual learning

The core of the PMoE framework is its ability to classify diverse flow regimes in an unsupervised manner, determining whether the incoming case belongs to a known flow scenario or represents a novel regime that requires model expansion.

As illustrated in figure 3, the PMoE router features a modular architecture, in which each router component adopts a standard autoencoder architecture following the design of Hinton & Salakhutdinov (2006), aiming to compress and reconstruct the feature space of a specific flow regime. The idea of learning internal representations through minimizing input reconstruction traces back to the backpropagation framework of Rumelhart *et al.* (1986). The network in this study consists of an encoder f_θ mapping the input \mathbf{x} to a latent representation \mathbf{z} , and a decoder g_ϕ reconstructing it as $\hat{\mathbf{x}}$. The network parameters of the encoder and the decoder shown in figure 3(a) are presented by θ and ϕ respectively. The training objective for the autoencoder is to minimize the reconstruction loss over the N sampled points, as

$$\mathbf{z} = f_\theta(\mathbf{x}), \quad \hat{\mathbf{x}} = g_\phi(\mathbf{z}), \quad \theta, \phi = \arg \min_{\theta, \phi} \mathcal{L}(\mathbf{x}, \hat{\mathbf{x}}). \quad (2.4)$$

Here, the reconstruction error $\mathcal{L}(\mathbf{x}, \hat{\mathbf{x}})$ is assessed as

$$\mathcal{L}(\mathbf{x}, \hat{\mathbf{x}}) = \frac{1}{N} \sum_j^N L_j = \frac{1}{N} \sum_j^N \sqrt{\frac{1}{M} \sum_i^M (\hat{x}_{i,j} - x_{i,j})^2}, \quad (2.5)$$

where for the j^{th} point, $x_{i,j}$ is the i^{th} component of its input feature vector, and $L_j = \sqrt{\frac{1}{M} \sum_{i=1}^M (\hat{x}_{i,j} - x_{i,j})^2}$ refers to its corresponding reconstruction error over the M features.

For every router component, a compact architecture is adopted, consisting of several hidden layers with moderate width to balance representational capacity and generalization as shown in figure 3(a). Leaky Rectified Linear Unit (LeakyReLU) (Maas *et al.* 2013) activations are employed between layers to introduce nonlinearity, and the Adam optimizer (Kingma & Ba 2015) is used with an initial learning rate of 10^{-2} . A step-based learning rate scheduler is employed, where the learning rate is reduced by a factor of 0.98 every 100 epochs to improve convergence stability. The number of training epochs is capped at 5000 based on empirical convergence studies, while an early-stopping strategy is employed to improve efficiency and mitigate overfitting. For all component trainings, the loss consistently reaches a plateau well before the maximum epoch count, and extending the training further does not yield noticeable performance improvement. After the training of the k^{th} router component C_k is converged, we set the 99.9th percentile of the reconstruction error of the training data as the corresponding threshold T_k , in order to eliminate the misleading influence of points with extreme distributions.

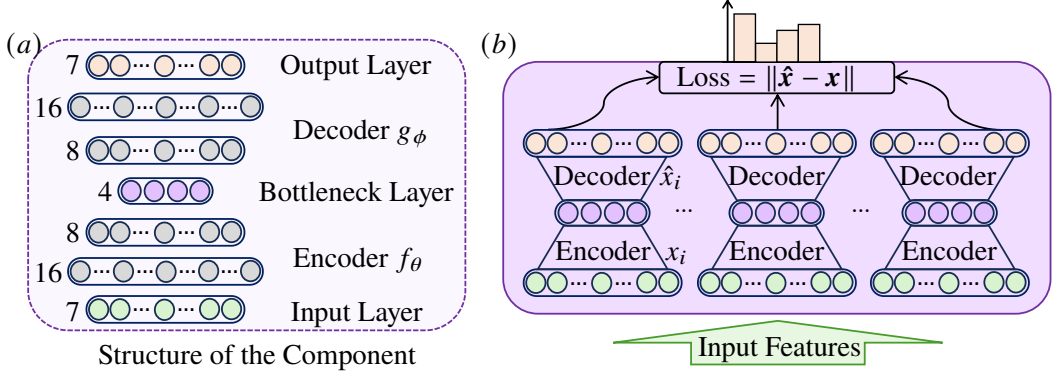


Figure 3. Structure of the router based on autoencoder. (a) Neural network architecture design for the autoencoder component. (b) The modular architecture of the router.

During the inference process, the router must determine if a new input flow belongs to a known regime or represents a novel physical scenario through the reconstruction error. For a new input case with N sampled points, a point j is considered recognized by component C_k if its local reconstruction error satisfies $L_j < T_k$. The global confidence level p_k of expert k regarding the current flow is defined as the relative frequency of recognized points

$$p_k = \frac{N_k}{N}, \quad \text{where } N_k = \sum_j^N \mathbb{I}(L_j < T_k), \quad (2.6)$$

where $\mathbb{I}(\cdot)$ is the indicator function.

The framework employs a *winner-takes-all* or top-1 gating strategy. The router selects the expert $E_{\mathcal{K}}$ corresponding to the component with the maximum confidence as

$$\mathcal{K} = \arg \max_k p_k. \quad (2.7)$$

However, activation is conditional and governed by a global acceptance threshold T_{accept} . When the maximum confidence $p_{\mathcal{K}}$ exceeds a threshold of $T_{\text{accept}} = 90\%$, the expert $E_{\mathcal{K}}$ will be activated. Conversely, if $p_{\mathcal{K}}$ falls below T_{accept} , the flow is deemed unknown, which triggers the continual learning process. In this case, a new autoencoder component C_{new} and a new expert E_{new} are initialized and trained on the new dataset. This modular design ensures isolation between old and new components during training, thus inherently overcoming catastrophic forgetting. Note while a threshold of $T_{\text{accept}} = 90\%$ is found to be effective for the distinct regimes in the present study, future industrial applications may require this hyperparameter to be tuned based on the desired sensitivity to novel flow physics.

The rationale for employing an autoencoder for flow classification rests on the premise that, the hierarchical importance of physical features varies significantly across different flow scenarios, which can be seen from the feature important analysis in appendix A. During the routing stage, an input feature matrix $\mathbf{X} \in \mathbb{R}^{N \times M}$ is compressed into a low-dimensional bottleneck representation $\mathcal{H}_\theta = f_\theta(\mathbf{X})$ to extract the feature combinations most critical for reconstructing the local flow physics. Following the information bottleneck (IB) principle proposed by Tishby *et al.* (2000), the training objective is formulated as

$$\min_\theta [I(\mathbf{X}; \mathcal{H}_\theta) - \beta I(\mathcal{H}_\theta; \mathbf{Y})], \quad (2.8)$$

where θ denotes the encoder parameters, $I(\cdot; \cdot)$ represents mutual information, and β governs the trade-off between compression and relevance. For the reconstruction task, the output matrix $\mathbf{Y} \in \mathbb{R}^{N \times M}$ is taken to be consistent with the input \mathbf{X} . The IB formulation implies the existence of a minimal informative feature subset $S \subseteq \{1, 2, \dots, M\}$ such that the sub-matrix $\mathbf{X}_S \in \mathbb{R}^{N \times |S|}$ satisfies

$$I(\mathbf{X}_S; \mathbf{Y}) = I(\mathbf{X}; \mathbf{Y}), \quad I(\mathbf{X}_{S'}; \mathbf{Y}) < I(\mathbf{X}; \mathbf{Y}), \quad \forall S' \subset S. \quad (2.9)$$

This implies that the autoencoder effectively isolates feature combinations that are strictly relevant to flow reconstruction. Consequently, for distinct flow scenarios, the network relies on different minimal subsets. This mechanism enables flow identification by exploiting the dependence of the latent representation \mathcal{H}_θ on flow-specific informative features. Note that the dimension of the latent bottleneck layer is a critical parameter which determines how much the input data can be compressed. We set the latent layer to have four nodes in the present study as shown in figure 3(a), which is based on a series of sensitivity tests.

2.2.3. Sparsely activated expert group with heterogeneous formulation

A distinct advantage of the PMoE framework is its support for heterogeneous expert formulations. Unlike data-driven models that typically enforce a single-form closure correction, e.g., a neural network predicting Reynolds stress anisotropy (Ling *et al.* 2016), the PMoE allows each expert E_k to adopt the mathematical structure best suited for its specific flow regime. This flexibility ensures that simple flows can be modelled by interpretable algebraic corrections, while complex non-equilibrium flows can leverage high-capacity neural networks.

In the present implementation, we utilize the Spalart–Allmaras (SA) model (Spalart & Allmaras 1992) as the baseline model. The standard transport equation for the modified eddy viscosity $\tilde{\nu}$ is given by

$$\frac{D\tilde{\nu}}{Dt} = \underbrace{C_{b1}\tilde{S}\tilde{\nu}}_{\mathcal{P}} + \underbrace{\frac{1}{\sigma} [\nabla \cdot ((\nu + \tilde{\nu})\nabla \tilde{\nu}) + C_{b2}(\nabla \tilde{\nu})^2]}_{\mathcal{T}} - \underbrace{C_{w1}f_w \left(\frac{\tilde{\nu}}{d}\right)^2}_{\mathcal{D}}, \quad (2.10)$$

where \mathcal{P} , \mathcal{T} , and \mathcal{D} represent the production, transport, and destruction terms, respectively. The standard definitions for the model constants (such as C_{b1} , C_{b2} , σ and C_{w1}) and closure functions like f_w are retained from Spalart & Allmaras (1992), and we only present the terms that will be modified here for brevity. In particular, the turbulent eddy viscosity is computed from $\nu_t = \tilde{\nu}f_{\nu1}$ and $f_{\nu1}$ is defined as

$$f_{\nu1} = \frac{\chi^3}{\chi^3 + c_{\nu1}^3}, \quad \chi \equiv \tilde{\nu}/\nu, \quad (2.11)$$

where $c_{\nu1} = 7.1$ and χ represents the ratio between $\tilde{\nu}$ and the molecular viscosity ν . Moreover, \tilde{S} is the modified vorticity magnitude. Within the PMoE framework, we demonstrate the integration of three distinct expert formulations.

Type I: parameter correction for wall-attached flows. For equilibrium boundary layers where the baseline model structure is sound but parameter calibration is suboptimal, the expert provides a scalar correction to existing coefficients. For the wall-attached expert E_1 , we employ a symbolic regression approach (Weatheritt & Sandberg 2016) to recalibrate the damping function $f_{\nu1}$ as suggested by Bin *et al.* (2023). The expert predicts a corrected functional form which replaces the standard definition in (2.11) to better capture the logarithmic layer velocity profile.

Type II: correction of production term for flow separation. For flows dominated by separation and strong pressure gradients, the equilibrium assumption in the linear eddy viscosity hypothesis often fails. Here, the expert E_2 is formulated as a neural network derived from the field inversion and machine learning (FIML) method (Parish & Duraisamy 2016). It imposes a spatially varying correction term β into the production term of the transport equation:

$$\mathcal{P}^* = \beta(\mathbf{x}) \cdot C_{b1} \tilde{S} \tilde{v}. \quad (2.12)$$

This multiplicative correction allows the model to locally suppress or enhance turbulence production in recirculation zones without altering the model behavior in the free stream.

Type III: constitutive relation modification for secondary flows. For corner flows where linear eddy viscosity models fail to predict secondary motions due to the isotropy assumption, the expert E_3 modifies the stress-strain relationship itself. We adopt a data-driven calibration of the quadratic constitutive relation (QCR) (Spalart 2000):

$$\tau_{ij, \text{QCR}} = \tau_{ij}^{\text{linear}} - C_{\text{cr1}}(\mathbf{x}) (O_{ik} \tau_{jk} + O_{jk} \tau_{ik}), \quad (2.13)$$

where O_{ik} is the normalized rotation tensor. Unlike the standard QCR where C_{cr1} is constant, the expert E_3 predicts a spatially varying C_{cr1} field to accurately capture corner vortices.

This modularity allows the PMoE framework to progressively integrate experts ranging from concise symbolic expressions to complex neural mappings without structural conflict, effectively decoupling the model architecture from the constraints of a single baseline formulation. This flexibility allows developers to select the most suitable expert design strategy for a given flow regime and to update or expand the expert group in step with advances in the literature, thereby further enhancing the practicality, extensibility, and efficiency of the framework.

3. Continuously learning PMoE model with various cases introduced progressively

To demonstrate the sustainable generalization capability of the PMoE framework, we employ a curriculum learning strategy. As shown in figure 4, we introduce flow regimes in an order of increasing physical complexity: free-shear turbulence, equilibrium wall-bounded flow, separated flow, and corner-induced secondary flow. This mimics an industrial workflow where a model must adapt to novel scenarios without discarding prior knowledge.

The evolution of the model is denoted by stages S_0 through S_3 , with the corresponding trained PMoE denoted as PMoE-S0, PMoE-S1, PMoE-S2 and PMoE-S3, respectively. At each stage, the router evaluates the novelty of the incoming data. We extract features from sampled points in the baseline RANS flow field, and construct input vector \mathbf{x} and matrix $\mathbf{X} \in \mathbb{R}^{N \times M}$, where $M = 7, N = 10000$ in our training process. The input data is then evaluated through the existing router modules. If the maximum confidence $p_{\mathcal{K}}$ falls below the acceptance threshold $T_{\text{accept}} = 90\%$, the system triggers the expansion mechanism: a new autoencoder component is trained to recognize the regime, and a specialized expert is trained to close the RANS equations. The specific datasets and their role in the curriculum are detailed in table 2. It should be noted that for each flow regime, only a portion of the working conditions are used for the training of router and experts, while the rest are left for model validation in § 4. The numerical setup of RANS calculation for each case is summarized in appendix B.

While completing the expansion of the router from PMoE-S0 to PMoE-S3, we also need to synchronously train the corresponding expert model for each newly identified flow

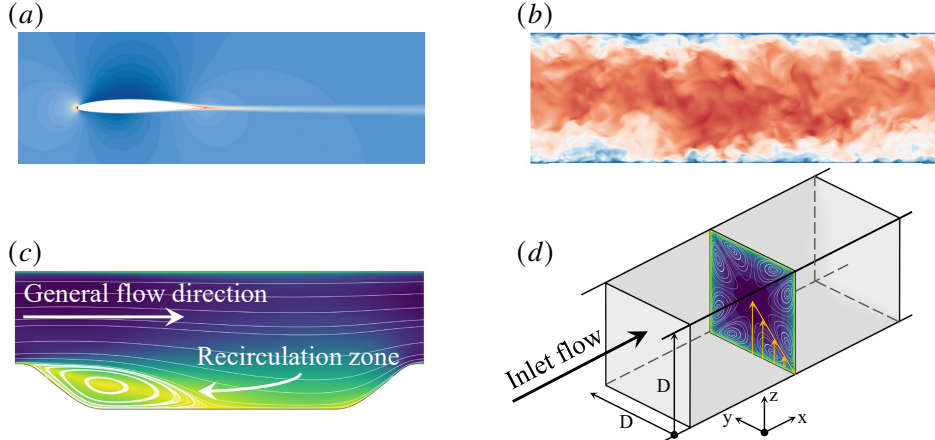


Figure 4. Schematic diagrams of typical examples of various flow regimes. (a) 2DANW. (b) Fully developed channel flow. (c) Periodic hill flow. (d) Square duct flow.

Flow Regime	Case	Abbreviation	Stages	Reference
Stage 0: Baseline	2D Airfoil Near-Wake	2DANW	training	Nakayama (1985)
Stage 1: wall-attached turbulence	Fully developed channel at $Re_\tau = 2000$	C2000	training	Lee & Moser (2015); Yamamoto & Tsuji (2018)
	Fully developed channel at $Re_\tau = 5200$	C5200	training	
	Fully developed channel at $Re_\tau = 8000$	C8000	validation	
Stage 2: separated flow	Periodic hill with $\alpha = 0.8$	PH0p8	validation	Xiao <i>et al.</i> (2020)
	Periodic hill with $\alpha = 1.0$	PH1p0	training	
	Periodic hill with $\alpha = 1.2$	PH1p2	validation	
	Periodic hill with $\alpha = 1.5$	PH1p5	validation	
Stage 3: corner flow	Square duct at $Re = 2500$	SD2500	training	Pinelli <i>et al.</i> (2010); Vinuesa <i>et al.</i> (2018)
	Square duct at $Re = 3500$	SD3500	validation	
	Square duct at $Re = 5693$	SD5693	training	

Table 2. Summary of flow cases used for training and validation.

regime. It should be particularly pointed out that the regimes are distinguished by the router automatically rather than pre-specified by humans during the training process.

3.1. Stage 0: Baseline initialization

The initial model, PMoE-S0, is established using the 2D Airfoil Near-Wake (2DANW) case. Detailed case configuration are referred to the NASA web page ¹, and the grid used for the present RANS calculations is given in appendix B. This regime represents simple free-shear turbulence where the standard SA model is known to perform adequately

¹Data available online at <https://turbmodels.larc.nasa.gov/airfoilwake/verif500c.html>

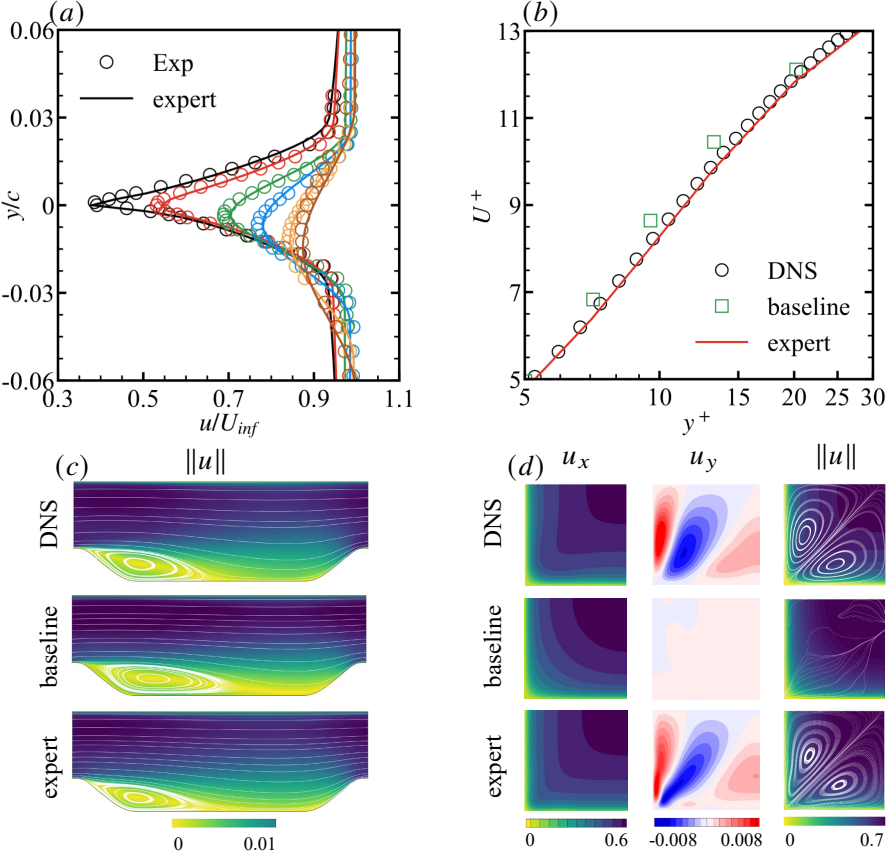


Figure 5. Velocity profiles and contours predicted by the baseline SA model, the expert model and high-fidelity data. (a) Expert for S0 trained by 2DANW. (b) Expert for S1 trained by C5200. (c) Expert for S2 trained by PH1p0. (d) Expert for S3 trained by SD2500 and SD5693.

	$S0$	$S0 \rightarrow S1$	$S1 \rightarrow S2$	$S2 \rightarrow S3$
New Regime	2DANW			
MAX confidence with existing router	—	C2000, C5200 0.0%	58.4% 56.7%	
Introduced Expert	SA Baseline	SR Expression	FI-NN	FI-NN
Confidence of new router component	99.9%	99.5%	93.5%	97.0%

Table 3. Progressive construction of the PMoE model.

(Bin *et al.* 2023). Consequently, we designate the SA model as baseline expert E_0 , and its performance in the 2DANW case is presented in figure 5(a). Furthermore, the first router component C_0 is trained on the wake features, establishing the baseline latent space distribution. As shown in table 3, the router identifies this regime with 99.9% confidence, serving as the anchor for future expansions.

3.2. Stage 1: Adaptation to wall-bounded turbulence

In the second phase, the model is exposed to fully developed turbulent channel flows at $Re_\tau = 2000$ and 5200. The grid sizes used for the present RANS calculations are provided in appendix B. When this data is fed into PMoE-S0, the router yields a confidence of 0.00% as presented in table 3, correctly identifying that the physics of the wall turbulence differs fundamentally from the free-shear wake.

This triggers the creation of a new expert E_1 . As discussed in §2.2.3, we employ symbolic regression to derive a correction for the damping function $f_{\nu 1}$. The resulting expert formulation is:

$$f_{\nu 1}^* = 0.985 \tanh\left(\frac{\chi^{1.3}}{31.1}\right). \quad (3.1)$$

Applying this expert to RANS calculations, the corrected model is able to provide more accurate wall-normal profiles compared to the baseline SA, agreeing well with the DNS result (Lee & Moser 2015) as shown in figure 5(b). Simultaneously, a new router component C_1 is trained. The updated model, PMoE-S1, subsequently recognizes the channel data with 99.5% confidence, effectively learning the wall-bounded regime while retaining Expert 0 for wakes.

3.3. Stage 2: Capturing flow separation

Most industrial flows exhibit features such as strong pressure gradients, streamline curvature and separation, which violate the equilibrium assumption underlying conventional RANS models. The periodic hill flow is usually adopted as a canonical benchmark for separated turbulence, as it combines adverse pressure gradients, separation and reattachment in a simple, well-defined geometry, with the accurate prediction of the separation bubble remaining a key modelling challenge. The Reynolds number of the periodic hill cases is set as 5600, consistent with DNS simulation (Xiao *et al.* 2020), and the hill slope defined by $\alpha = l/h$ varies across cases, where l and h are the hill width and height, respectively.

The curriculum thus proceeds to the periodic hill case with $\alpha = 1.0$ as shown in table 2. The PMoE-S1 router produces a maximum confidence of 58.4% as presented in table 3. Note that this relatively high-level of confidence is likely due to shared wall-bounded features. Nevertheless, it falls below the 90% threshold, flagging the regime as novel.

To address the non-equilibrium physics in the recirculation bubble, we train a new expert E_2 using the FIML method. This expert injects a source term $\beta(x)$ into the production term as presented in equation 2.12. Specifically, the flow field inversion based on the adjoint method employs a framework named DAFoam (He *et al.* 2018, 2020). Subsequently, the mapping from the input features to the beta parameter field is trained via a three-layer fully connected feed-forward network implemented using PyTorch (Paszke *et al.* 2019). Prior to training, all input features are normalized to the range of $[0, 1]$ using min–max scaling, in order to improve numerical conditioning during optimization and promote stable and efficient training. The dataset was randomly divided into training and testing subsets, with an 80% to 20% ratio for training and testing, respectively. The model contains seven input features, two hidden layers with 64 and 32 neurons, and a single scalar output, employing Rectified Linear Unit (ReLU) (Glorot *et al.* 2011) activation between layers to introduce nonlinearity. The network is trained using the Adam optimizer with a cosine-annealed learning-rate schedule, combined with an adaptive reduction strategy triggered by validation-loss plateaus, which enhances convergence robustness. The loss function used during training is constructed based on mean-squared-error (MSE). The compact structure

provides sufficient representational power for nonlinear feature interactions while limiting overfitting risk.

As shown in figure 5(c), the trained separation flow expert can more accurately capture the phenomena of separation and reattachment, while the estimation of the separation bubble size by the basic SA model is significantly larger than that of the expert model and DNS results. Furthermore, upon integrating E_2 and its corresponding router component, the identification confidence for separated flows rises to 93.5%, yielding model PMoE-S2.

3.4. Stage 3: Modelling corner-induced anisotropy

Finally, the model encounters the square duct flow at $Re = 2500, 5693$. This case is physically distinct due to the secondary motions in the corner region, which are impossible for linear eddy viscosity models. The training data are obtained from published DNS simulations (Pinelli *et al.* 2010; Vinuesa *et al.* 2018). The Reynolds number is based on the half edge length $h = D/2$ of the square duct and the bulk velocity U_b as shown in figure 4(d).

The PMoE-S2 router yields a confidence of 56.7% as presented in table 3, again triggering expansion. A new expert 3 E_3 is then trained to predict the non-linear stress coefficient $C_{cr1}(\mathbf{x})$ in the QCR formulation in equation 2.13. The same network architecture and tools as in § 3.3 are used, so we will not repeat the description here. As shown in the figure 5(d), the trained expert model successfully captures the generation of secondary flow, while the baseline SA model is unable to calculate the secondary flow. The final model, PMoE-S3, achieves a recognition confidence of 97.0% for this regime.

4. Model validation

The validation of the PMoE framework focuses on three critical performance metrics: the interpretability of the unsupervised routing, the prevention of catastrophic forgetting on previously learned regimes, and the generalization capability to unseen cases. All results presented herein utilize the final PMoE-S3 model to demonstrate its cumulative capabilities.

4.1. Validation for the PMoE router

A prerequisite for reliable expert selection is the router's ability to distinguish flow regimes based on local RANS features. We analyze the four-dimensional latent space of the autoencoder components using the Mahalanobis distance (Mahalanobis 1936), D_M , which measures the distance between a point z and a distribution with mean μ and covariance Σ :

$$D_M^2(z) = (z - \mu)^T \Sigma^{-1} (z - \mu). \quad (4.1)$$

Unlike the Euclidean distance, D_M accounts for the correlation structure of the learned representations. Based on this metric, we compute both the intra-cluster dispersion, which quantifies the compactness of samples within a regime, and the inter-cluster dispersion measuring the separation between regime centroids, as illustrated in figure 6. The ratio between the averaged inter- and intra-cluster dispersions is adopted as a diagnostic indicator of the latent-space organization. A high ratio implies that different flow regimes are topologically distinct within the component's latent space, whereas a low ratio suggests possible overlap.

This *a posteriori* analysis is carried out for all four components. Each component is exposed to data from all four flow regimes to assess its discriminative behavior, and table 4 summarizes these statistics. The intra-cluster dispersion remains consistent as

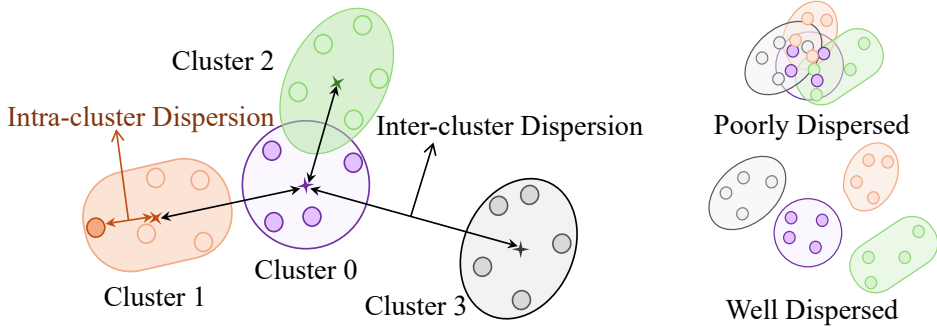


Figure 6. Schematic illustration of intra- and inter-cluster dispersion based on the Mahalanobis distance.

Dispersion	C_0 Baseline Flow	C_1 Wall-attached Flow	C_2 Separated Flow	C_3 Corner Flow
Average intra-cluster	1.8207	1.8383	1.8438	1.6947
Average inter-cluster	6.6845	6.3698	7.6183	7.8923
inter-cluster/intra-cluster	3.6713	3.4650	4.1319	4.6569

Table 4. Dispersion analysis of the latent space clusters using Mahalanobis distance.

≈ 1.8 across all components, indicating that the autoencoders compress different flow regimes with comparable efficiency. Furthermore, the ratios between the averaged inter- and intra-cluster dispersions are also presented, and all four components exhibit ratios exceeding 3.4, indicating that the corresponding clusters have little overlap as illustrated by the well-separated configuration in figure 6. Although the router decision is ultimately based on the reconstruction error along the full encoder–decoder pathway, the *a posteriori* latent-space analysis still provides an interpretable metric for its behavior, as the observed clustering patterns reflect the feature representations that govern reconstruction quality and hence routing outcomes. This mechanism, combined with the competitive winner-takes-all strategy, ensures robust classification. As evidenced in table 5, the router achieves $> 90\%$ classification accuracy on the validation sets, confirming that the present router successfully distinguishes the tested regimes.

4.2. Prevention of catastrophic forgetting via in-distribution tests

A primary failure mode in continual learning is catastrophic forgetting, where optimizing for new tasks degrades performance on previous ones (French 1999). To assess whether the current PMoE framework is able to avoid catastrophic forgetting, we apply the final PMoE-S3 model back to the initial training cases.

Figure 7(a) presents the wake velocity profiles for the 2DANW case (Stage 0), with each color representing a different observation position: black for $x/c = 1.01$, red for $x/c = 1.01$, black for $x/c = 1.05$, green for $x/c = 1.20$, blue for $x/c = 1.40$, yellow for $x/c = 1.80$ and brown for $x/c = 2.19$. Despite the model undergoing three subsequent expansions involving wall-bounded and secondary flows, the prediction for the free-shear wake remains virtually identical to the baseline SA model and agrees well with experimental

Case	Unknown	C_0 Baseline Flow	C_1 Wall-attached Flow	C_2 Separated Flow	C_3 Corner Flow
ANW	0.0%	99.7%	0.3%	0.0%	0.0%
C2000	0.2%	0.0%	98.1%	0.5%	1.2%
C5200	0.0%	0.0%	99.4%	0.0%	0.6%
C8000	3.9%	0.0%	94.5%	1.3%	0.3%
PH0p8	0.3%	0.0%	5.7%	91.6%	2.5%
PH1p0	0.1%	0.0%	5.4%	91.5%	3.0%
PH1p2	0.1%	0.0%	4.8%	92.0%	3.2%
PH1p5	0.2%	0.0%	4.7%	91.9%	3.2%
SD2500	0.4%	0.0%	0.3%	0.0%	99.3%
SD3500	0.5%	0.0%	0.0%	0.2%	99.3%
SD5693	0.0%	0.0%	2.2%	0.8%	97.0%

Table 5. Confidence distribution of the PMoE-S3 router over different components for all flow cases.

data. This confirms that the modular router successfully shields the baseline expert E_0 from interference.

Similarly, figures 7(b) and 7(c) show the mean velocity profiles extracted from the channel flow cases at $Re_\tau = 2000$ and $Re_\tau = 5200$ (Stage 1), while figure 7(d) and 7(e) present the periodic hill at $\alpha = 1.0$ (Stage 2). The final PMoE-S3 model retains the specialized accuracy of experts E_1 and E_2 in according tests. Particularly in the periodic hill case, the baseline model predicts a delayed reattachment near $x/h = 7.0$, whereas the PMoE model correctly captures the recirculation bubble size, matching the DNS reattachment at $x/h \approx 5.0$.

The capability of the final model PMoE-S3 for trained square duct ($Re = 2500$) is shown in figure 7(f–h). Figure 7(f) and 7(g) show the velocity profiles at $z/h = 0.3, h = D/2$, while the figure 7(h) represents $y/h = 0.25, 0.5, 0.75$ and 1.0 from left to right just as the yellow arrows shown in figure 4(d). The square duct case contains typical corner-induced secondary flow, which cannot be characterized by the SA model based on linear eddy viscosity. The results of PMoE-S3, however, have a significant improvement compared to the baseline model. This suggests that the trained PMoE-S3 model can effectively represent the secondary flow in the non-flow direction due to the introduction of nonlinear correction based on QCR. Moreover, figures 7(i–k) present the results of the SD5693 case. The performance of PMoE-S3 remains excellent, with significant improvements in both flow velocity and secondary flow representation compared to the baseline.

4.3. Generalization to unseen cases

The robustness of the PMoE-S3 model is further tested against cases never seen during training. The mean velocity profiles of all the cases are shown in figure 8. Compared with the cases in § 4.2, these new tests evaluate the model’s generalization ability to different Reynolds numbers and periodic hill geometries.

The model is applied to a channel flow at $Re_\tau = 8000$ and a square duct at $Re = 3500$. In both cases, the Reynolds numbers are different from the specific training conditions. The router successfully maps these flows to Experts E_1 and E_3 , respectively, as shown in table 5. The velocity profiles show excellent agreement with DNS data, indicating that the learned corrections, including the damping function modification in E_1 and the QCR coefficient field in E_3 , capture the underlying physics rather than merely overfitting the training data.

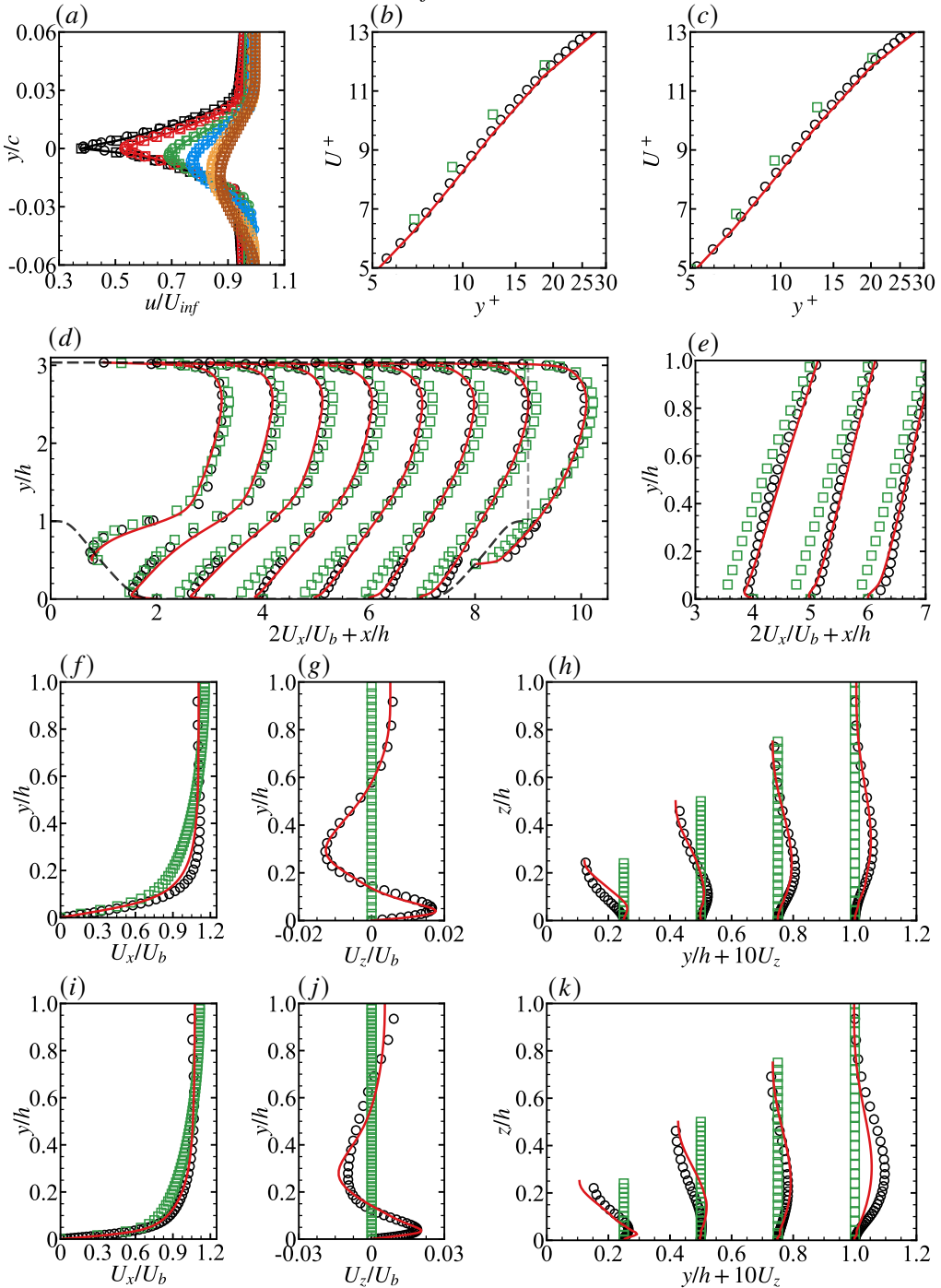


Figure 7. Mean velocity profiles for trained cases. (a) 2DANW (colors indicate streamwise locations). (b) C2000. (c) C5200. (d, e) PH1p0. (f-h) SD2500. (i-k) SD5693. Symbols denote: \circ DNS/Experimental data; \blacksquare Baseline SA; $\textcolor{red}{—}$ PMoE-S3.

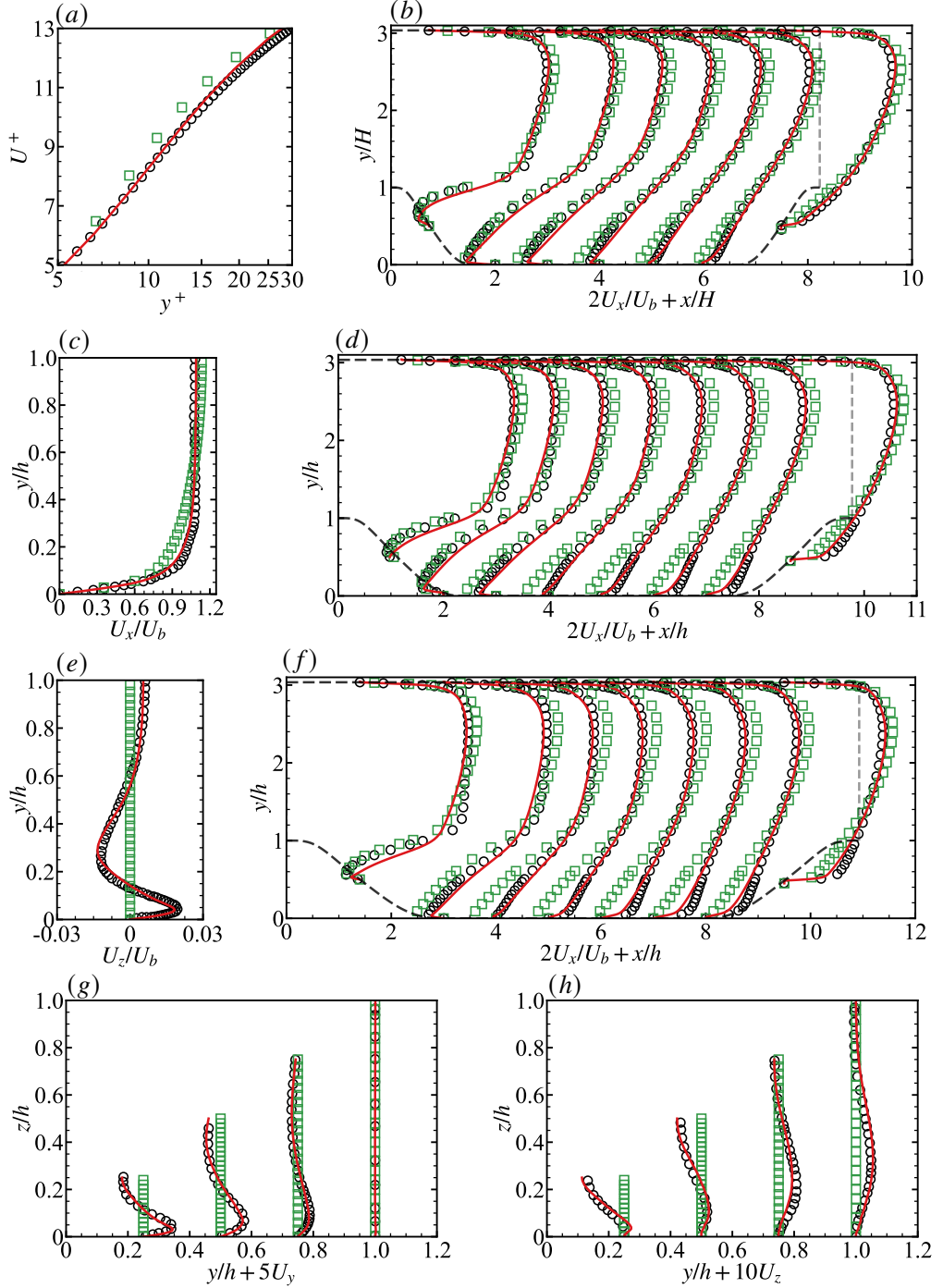


Figure 8. Mean velocity profiles for unseen cases. (a) C8000. (b) PH0p8. (d) PH1p2. (f) PH1p5. (c), (e), (g), (h) SD3500. Symbols denote: \circ DNS/Experimental data; \square Baseline SA; $\textcolor{red}{—}$ PMoE-S3.

We further test the periodic hill flows with varying slopes $\alpha = \{0.8, 1.2, 1.5\}$. These geometric changes significantly alter the adverse pressure gradient and the separation bubble size. As shown in figures 8(b, d, f), the PMoE-S3 model consistently outperforms the baseline, despite that the model has only been trained for the $\alpha = 1.0$ case. Similar to the conclusion drawn from § 4.2, the baseline SA model overestimates the size of the separation bubble in the lower hill area, while the PMoE-S3 model shows much better agreement with the result of DNS. This suggests that the FIML-trained expert E_2 has learned a generalized correction for separation control that is robust to geometric deformation.

Up to now, the PMoE-S3 model has achieved the recognition of various flow regimes and has significantly improved its performance compared to the baseline model. The verification results show that PMoE-S3 successfully overcomes catastrophic forgetting and achieves good scalability. Even after subsequent training with multiple sets of complex examples, it can still maintain a high level of previous capabilities.

4.4. Computational efficiency

A key advantage of the PMoE framework is its low computational cost during inference. As the model expands through continual learning, additional experts are introduced and the router acquires new components. However, owing to the sparse-activation mechanism, only a subset of experts is invoked at inference time. To provide a quantitative assessment of the computational overhead, we performed full-process tests using both the baseline SA model and the PMoE-S3 model on identical cases ², and the wall-clock time results are summarised in table 6. For all tests, the computational grid and the total number of iteration steps were kept fixed across models. Across all tests presented in the table, the routing time of the PMoE-S3 model remains below 10 seconds, demonstrating that the router is sufficiently lightweight and its overhead is negligible compared with the flow simulation itself. Furthermore, for all the examples, when using the final PMoE-S3 model, the total simulation time increases by only 0.15% ~ 4.0%, indicating that the inclusion of additional experts does not introduce a significant computational cost. This confirms that the PMoE framework offers improved accuracy with a marginal computational penalty, making it viable for industrial-scale CFD applications.

5. Conclusions

In this work, we propose a progressive modular mixture-of-experts framework, termed PMoE, to address generalization and continual learning in data driven RANS turbulence modelling. The framework is based on a successively trainable autoencoder based similarity router that enables the progressive introduction of specialised turbulence model experts as new flow regimes emerge. Using training data covering four representative regimes, namely baseline airfoil wakes, wall-attached flows, separated flows and corner-induced secondary flows, we construct the PMoE-S3 model and demonstrate its ability to deliver accurate predictions for both seen and unseen test cases.

A key advantage of the proposed framework lies in its support for continual learning without catastrophic forgetting. New flow regimes can be incorporated by adding dedicated experts and router component, while previously trained components remain unchanged, preserving established predictive capabilities. Moreover, the modular design of PMoE allows experts of fundamentally different forms to coexist within a single framework, offering the flexibility to integrate turbulence models based on different formulations

²All tests were conducted on a system equipped with an Intel® Xeon® Gold 6530 CPU and an NVIDIA® AD102 (GeForce RTX 4090) GPU.

	Case	Routing	Simulation	Total
Baseline	ANW	–	1943s	1943s
PMoE-S3		9.82s	1936s	1945.82s
Increase Ratio		–	-0.36%	0.15%
Baseline	C5200	–	425s	425s
PMoE-S3		8.01s	434s	442.01s
Increase Ratio		–	2.12%	4.00%
Baseline	PH1p5	–	2810s	2810s
PMoE-S3		6.80s	2884s	2890.80s
Increase Ratio		–	2.63%	2.88%
Baseline	SD5693	–	2077s	2077s
PMoE-S3		9.29s	2124s	2133.29s
Increase Ratio		–	2.26%	2.71%

Table 6. Comparison of computational wall-clock time between the baseline SA model and PMoE-S3 model.

and assumptions as needed. Importantly, the training procedure relies on unsupervised feature extraction through the autoencoder-based router, making the framework particularly well suited to industrial workflows where labeled data and repeated full retraining are often impractical. Beyond its demonstrated performance, PMoE provides a scalable and extensible platform for RANS modelling. Owing to the sparse activation mechanism, model expansion does not lead to a proportional increase in computational cost during inference, which is essential for industrial CFD applications. Its plug-and-play structure enables modular updates and reduces both development and deployment costs, while its extensibility allows the turbulence modelling community to contribute new experts targeting previously unexplored flow regimes, establishing a living framework that can evolve alongside advances in modelling strategies.

Building on the modular and extensible nature of the framework, future developments may incorporate experts based on alternative turbulence closures, such as the $k-\omega$ shear stress transport (SST) model (Menter 1994) or Reynolds stress models (Launder *et al.* 1975), to broaden its applicability. For more complex flows, region aware routing is expected to become increasingly important for applying different experts within different spatial zones. Although the current set of input features is sufficient for distinguishing the flow regimes examined here, further enrichment of the feature representation may be required as additional flow types are considered.

Acknowledgements. This work has been supported by the National Natural Science Foundation of China (Grant Nos. 12588201, 12572247 and 12432010).

Declaration of interests. The authors report no conflict of interest.

Appendix A. Feature importance analysis

Feature importance analysis is commonly employed to improve the interpretability of neural networks by quantifying the contribution of each input feature to the model prediction (Breiman 2001). In this work, to explore whether the importance distribution of different features varies in various flow regimes and thereby demonstrate the feasibility of identifying flow types based on feature importance, it is necessary to conduct a feature importance analysis.

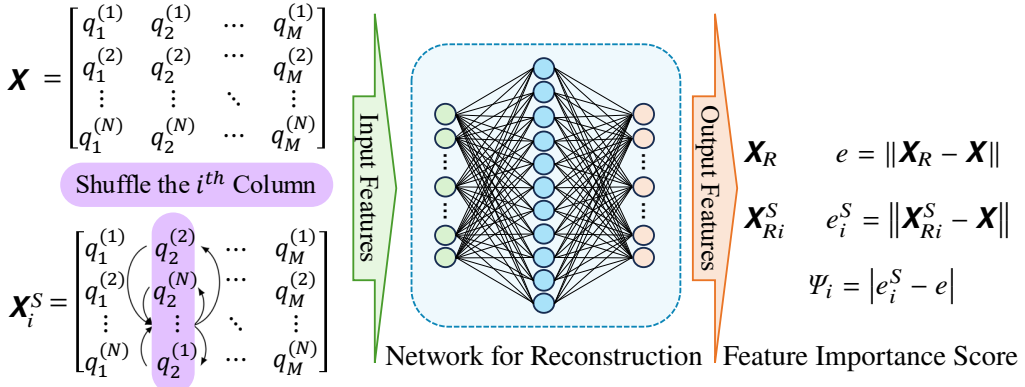


Figure 9. Schematic illustration of the formulation and computational procedure of the PFI.

Among such approaches, PFI provides a model-agnostic assessment of the sensitivity of a fitted model to individual features using a prescribed tabular dataset (Fisher *et al.* 2019; Mandler & Weigand 2023). It is achieved by shuffling values of a single feature and subsequently assessing the consequent deterioration in the model performance. This approach can determine the extent to which the model depends on a specific feature by disrupting the intrinsic connection between the input features and the model prediction. The procedure of the PFI method is illustrated in figure 9. The inputs include a DNN used for reconstruction, an input feature matrix $\mathbf{X} \in \mathbb{R}^{N \times M}$ comprising M features and N sampling points, and the corresponding targets, which coincide with \mathbf{X} for this reconstruction task. For each feature q_i , a permuted matrix \mathbf{X}_i^S is generated by shuffling the i^{th} column of \mathbf{X} , and the reconstruction error e_i^S is recomputed as $\|\mathbf{X}_{Ri}^S - \mathbf{X}\|$. The importance associated with each feature q_i is defined as Ψ_i , the change in error induced by permutation, providing a quantitative measure of the model's sensitivity to that feature. All features are analyzed in this manner, and the ranking is obtained from repeated trials with averaged results to minimize statistical variability.

To eliminate the interference caused by network capacity, we choose an MLP network with sufficient network parameters to test whether the four types of flowing data we adopt have different order of feature importance in the reconstruction task. PFI results are shown in figure 10. Features with higher importance scores are considered more informative. The four flow regimes exhibit distinct importance profiles, indicating that different subsets of features govern the reconstruction. For example, free-shear turbulence relies primarily on q_1, q_2, q_3 and q_5 , whereas separated flows depend more strongly on q_2, q_3, q_5 , and q_6 . These class-dependent importance patterns lead to substantially different parameter distributions when training the modular experts of the router network. This explains why the approach of using reconstruction errors as the identification basis can effectively distinguish different flow types of data, and still maintain a high accuracy rate after modular expansion.

Appendix B. Case setting

Numerical simulations in this paper are performed using the open-source computational framework OpenFOAM (Open Source Field Operation and Manipulation, version 2012). The built-in solver simpleFoam is primarily used in this work to solve the RANS equations coupled with specialized expert models. The SA baseline model mentioned in this article refers to the model and default parameter settings presented by Spalart & Allmaras (1992). Grids and computation domain are shown in table 7.

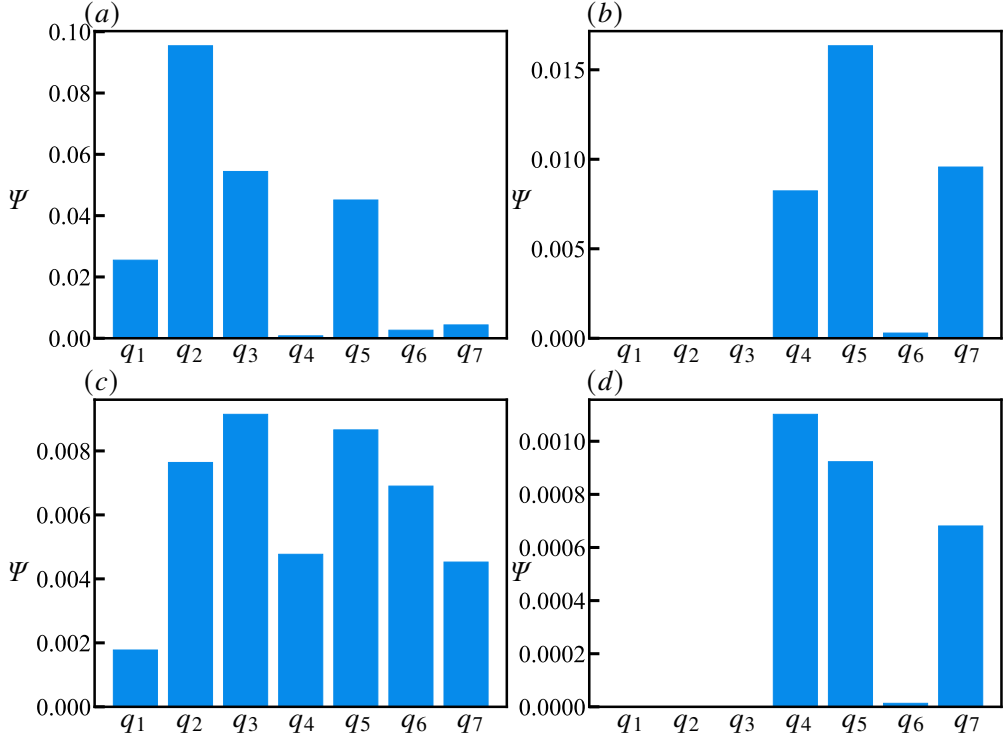


Figure 10. Feature importance scores obtained from the PFI for the four regimes of flow. (a) Baseline flow (airfoil wake). (b) Wall-attached flow. (c) Separated flow. (d) Corner flow.

Case	Box	Grid
ANW	$1000c \times 1000c$	$337 \times 449, 513 \times 225$
C2000	$4\pi h \times 2h$	250×100
C5200	$4\pi h \times 2h$	500×200
C8000	$4\pi h \times 2h$	800×320
PH0p8	$8.23h \times 3.036h$	99×149
PH1p0	$9.0h \times 3.036h$	99×149
PH1p2	$9.77h \times 3.036h$	99×149
PH1p5	$10.93h \times 3.036h$	99×149
SD2500	$2.5D \times D \times D$	$75 \times 48 \times 48$
SD3500	$2.5D \times D \times D$	$75 \times 48 \times 48$
SD5693	$2.5D \times D \times D$	$75 \times 48 \times 48$

Table 7. Computational domains and grid resolutions for all cases considered in this study.

REFERENCES

AMARLOO, A., RINCÓN, M.J., RECLARI, M. & ABKAR, M. 2023 Progressive augmentation of turbulence models for flow separation by multi-case computational fluid dynamics driven surrogate optimization. *Phys. Fluids* **35** (12), 125154.

ARRANZ, G., LING, Y., COSTA, S., GOC, K. & LOZANO-DURÁN, A. 2024 Building-block-flow computational model for large-eddy simulation of external aerodynamic applications. *Commun. Eng.* **3** (1), 127.

BIN, Y., HUANG, G. & YANG, X.I.A. 2023 Data-enabled recalibration of the Spalart–Allmaras model. *AIAA J.* **61** (11), 4852–4863.

BREIMAN, L. 2001 Random forests. *Machine learning* **45** (1), 5–32.

BRUNTON, S.L., NOACK, B.R. & KOUMOUTSAKOS, P. 2020 Machine learning for fluid mechanics. *Ann. Rev. Fluid Mech.* **52**, 477–508.

BUSH, R.H., CHYCZEWSKI, T.S., DURAISAMY, K., EISFELD, B., RUMSEY, C.L. & SMITH, B.R. 2019 Recommendations for future efforts in RANS modeling and simulation. In *Proc. AIAA SciTech 2019*, p. 0317.

CHERROUD, S., MERLE, X., CINNELLA, P. & GLOERFELT, X. 2025 Space-dependent aggregation of stochastic data-driven turbulence models. *J. Comp. Phys.* **527**, 113793.

DAI, D., DENG, C., ZHAO, C., XU, R.X., GAO, H., CHEN, D., LI, J., ZENG, W., YU, X., WU, Y., XIE, Z., LI, Y.K., HUANG, P., LUO, F., RUAN, C., SUI, Z. & LIANG, W. 2024 DeepSeekMoE: Towards ultimate expert specialization in mixture-of-experts language models. In *Proc. 62nd Annu. Meet. Assoc. Comput. Linguist. (ACL)*, pp. 1280–1297.

DU, N., HUANG, Y., DAI, A.M., TONG, S., LEPIKHIN, D., XU, Y., KRIKUN, M., ZHOU, Y., YU, A.W., FIRAT, O. & OTHERS 2022 Glam: Efficient scaling of language models with mixture-of-experts. In *Proc. Int. Conf. Mach. Learn.*, pp. 5547–5569.

DURAISAMY, K., IACCARINO, G. & XIAO, H. 2019 Turbulence modeling in the age of data. *Ann. Rev. Fluid Mech.* **51**, 357–377.

DURAISAMY, K., ZHANG, Z.J. & SINGH, A.P. 2015 New approaches in turbulence and transition modeling using data-driven techniques. In *Proc. 53rd AIAA Aerospace Sci. Meet.*, p. 1284.

FANG, Y., ZHAO, Y., WASCHKOWSKI, F., OOI, A.S.H. & SANDBERG, R.D. 2023 Toward more general turbulence models via multicase computational-fluid-dynamics-driven training. *AIAA J.* **61** (5), 2100–2115.

FEDUS, W., ZOPH, B. & SHAZER, N. 2022 Switch transformers: scaling to trillion parameter models with simple and efficient sparsity. *J. Mach. Learn. Res.* **23** (120), 1–39.

FISHER, A., RUDIN, C. & DOMINICI, F. 2019 All models are wrong, but many are useful: Learning a variable's importance by studying an entire class of prediction models simultaneously. *J. Mach. Learn. Res.* **20** (177), 1–81.

FRENCH, R.M. 1999 Catastrophic forgetting in connectionist networks. *Trends in cognitive sciences* **3** (4), 128–135.

GLOROT, X., BORDES, A. & BENGIO, Y. 2011 Deep sparse rectifier neural networks. In *Proc. Int. Conf. Artif. Intell. Statist.*, pp. 315–323.

GORLE, C., EMORY, M. & IACCARINO, G. 2012 RANS modeling of turbulent mixing for a jet in supersonic cross flow: model evaluation and uncertainty quantification. In *THMT-12. Proceedings of the Seventh International Symposium On Turbulence Heat and Mass Transfer*, pp. 1794–1797.

HE, P., MADER, C.A., MARTINS, J.R. & MAKI, K.J. 2018 An aerodynamic design optimization framework using a discrete adjoint approach with OpenFOAM. *Comp. Fluids* **168**, 285–303.

HE, P., MADER, C.A., MARTINS, J.R. & MAKI, K.J. 2020 Dafoam: An open-source adjoint framework for multidisciplinary design optimization with OpenFOAM. *AIAA J.* **58** (3), 1304–1319.

HINTON, G.E. & SALAKHUTDINOV, R.R. 2006 Reducing the dimensionality of data with neural networks. *Science* **313** (5786), 504–507.

JACOBS, R.A., JORDAN, M.I., NOWLAN, S.J. & HINTON, G.E. 1991 Adaptive mixtures of local experts. *Neural Computation* **3** (1), 79–87.

JORDAN, M.I. & JACOBS, R.A. 1994 Hierarchical mixtures of experts and the EM algorithm. *Neural Computation* **6** (2), 181–214.

KINGMA, D.P. & BA, J. 2015 Adam: A method for stochastic optimization. *Proc. Int. Conf. Learn. Represent.* pp. 1–15.

LAUNDER, B.E., REECE, G.J. & RODI, W. 1975 Progress in the development of a Reynolds-stress turbulence closure. *J. Fluid Mech.* **68** (3), 537–566.

LAUNDER, B.E. & SHARMA, B.I. 1974 Application of the energy-dissipation model of turbulence to the calculation of flow near a spinning disc. *Lett. Heat Mass Transf.* **1** (2), 131–137.

LEE, M. & MOSER, R.D. 2015 Direct numerical simulation of turbulent channel flow up to $Re_\tau = 5200$. *J. Fluid Mech.* **774**, 395–415.

LING, J., KURZAWSKI, A. & TEMPLETON, J. 2016 Reynolds averaged turbulence modelling using deep neural networks with embedded invariance. *J. Fluid Mech.* **807**, 155–166.

LING, J. & TEMPLETON, J. 2015 Evaluation of machine learning algorithms for prediction of regions of high Reynolds averaged Navier Stokes uncertainty. *Phys. Fluids* **27** (8), 085103.

LOZANO-DURÁN, A. & BAE, H.J. 2023 Machine learning building-block-flow wall model for large-eddy simulation. *J. Fluid Mech.* **963**, A35.

MAAS, A.L., HANNUN, A.Y., Ng, A.Y. & OTHERS 2013 Rectifier nonlinearities improve neural network acoustic models. In *Proc. Int. Conf. Mach. Learn.*, p. 3.

MAHALANOBIS, P.C. 1936 On the generalised distance in statistics. *Proceedings of the National Institute of Science of India* **2**, 49–55.

MANDLER, H. & WEIGAND, B. 2023 Feature importance in neural networks as a means of interpretation for data-driven turbulence models. *Comp. Fluids* **265**, 105993.

MENTER, F.R. 1994 Two-equation eddy-viscosity turbulence models for engineering applications. *AIAA J.* **32** (8), 1598–1605.

MENTER, F.R. & MATYUSHENKO, A. 2025 Generalized k - ω (GEKO) two-equation turbulence model. *AIAA J.* **63** (11), 4590–4606.

NAKAYAMA, A. 1985 Characteristics of the flow around conventional and supercritical airfoils. *J. Fluid Mech.* **160**, 155–179.

OULGHELOU, M., CHERROUD, S., MERLE, X. & CINNELLÀ, P. 2025 Machine-learning-assisted blending of data-driven turbulence models. *Flow Turbul. Combust.* pp. 1–38.

PARISH, E.J. & DURAISAMY, K. 2016 A paradigm for data-driven predictive modeling using field inversion and machine learning. *J. Comp. Phys.* **305**, 758–774.

PASZKE, A., GROSS, S., MASSA, F., LERER, A., BRADBURY, J., CHANAN, G., KILLEEN, T., LIN, Z., GIMELSHEIN, N., ANTIGA, L. & OTHERS 2019 Pytorch: An imperative style, high-performance deep learning library **32**.

PINELLI, A., UHLMANN, M., SEKIMOTO, A. & KAWAHARA, G. 2010 Reynolds number dependence of mean flow structure in square duct turbulence. *J. Fluid Mech.* **644**, 107–122.

RUMELHART, D.E., HINTON, G.E. & WILLIAMS, R.J. 1986 Learning representations by back-propagating errors. *Nature* **323** (6088), 533–536.

RUMSEY, C.L. 2014 Turbulence modeling verification and validation. In *Proc. 52nd AIAA Aerospace Sci. Meet.*, p. 0201.

RUMSEY, C.L. & COLEMAN, G.N. 2022 NASA symposium on turbulence modeling: Roadblocks, and the potential for machine learning. Technical report. Langley Research Center, Hampton, VA, USA.

SANDBERG, R.D. & ZHAO, Y. 2022 Machine-learning for turbulence and heat-flux model development: A review of challenges associated with distinct physical phenomena and progress to date. *Int. J. Heat Fluid Flow* **95**, 108983.

SCHMELZER, M., DWIGHT, R.P. & CINNELLÀ, P. 2020 Discovery of algebraic Reynolds-stress models using sparse symbolic regression. *Flow Turbul. Combust.* **104** (2), 579–603.

SHAZEER, N., MIRHOSEINI, A., MAZIARZ, K., DAVIS, A., LE, Q., HINTON, G. & DEAN, J. 2017 Outrageously large neural networks: The sparsely-gated mixture-of-experts layer. In *Proc. Int. Conf. Learn. Represent.*, pp. 1–19.

SPALART, P.R. 2000 Strategies for turbulence modelling and simulations. *Int. J. Heat Fluid Flow* **21** (3), 252–263.

SPALART, P.R. & ALLMARAS, S.R. 1992 A one-equation turbulence model for aerodynamic flows. In *30th Aerospace Sciences Meeting and Exhibit*, p. 439.

TISHBY, N., PEREIRA, F.C. & BIALEK, W. 2000 The information bottleneck method. *arXiv preprint physics/0004057*.

VINUESA, R., SCHLATTER, P. & NAGIB, H.M. 2018 Secondary flow in turbulent ducts with increasing aspect ratio. *Phys. Rev. Fluids* **3** (5), 054606.

WANG, J., WU, J. & XIAO, H. 2017 Physics-informed machine learning approach for reconstructing reynolds stress modeling discrepancies based on DNS data. *Phys. Rev. Fluids* **2**, 034603.

WEATHERITT, J. & SANDBERG, R. 2016 A novel evolutionary algorithm applied to algebraic modifications of the RANS stress-strain relationship. *J. Comp. Phys.* **325**, 22–37.

WILCOX, D.C. 2008 Formulation of the k - ω turbulence model revisited. *AIAA J.* **46** (11), 2823–2838.

WU, C., ZHANG, X.-L., XU, D. & HE, G. 2025 A framework for learning symbolic turbulence models from indirect observation data via neural networks and feature importance analysis. *J. Comp. Phys.* **537**, 114068.

WU, C. & ZHANG, Y. 2023 Enhancing the shear-stress-transport turbulence model with symbolic regression: A generalizable and interpretable data-driven approach. *Phys. Rev. Fluids* **8**, 084604.

XIAO, H., WU, J.-L., LAIZET, S. & DUAN, L. 2020 Flows over periodic hills of parameterized geometries: A dataset for data-driven turbulence modeling from direct simulations. *Comp. Fluids* **200**, 104431.

XIAO, H., WU, J.-L., WANG, J.-X., SUN, R. & ROY, C.J. 2016 Quantifying and reducing model-form uncertainties

in Reynolds-averaged Navier–Stokes simulations: A data-driven, physics-informed Bayesian approach. *J. Comp. Phys.* **324**, 115–136.

YAMAMOTO, Y. & TSUJI, Y. 2018 Numerical evidence of logarithmic regions in channel flow at $Re_\tau = 8000$. *Phys. Rev. Fluids* **3** (1), 012602.

YIN, Y., YANG, P., ZHANG, Y., CHEN, H. & FU, S. 2020 Feature selection and processing of turbulence modeling based on an artificial neural network. *Phys. Fluids* **32** (10).

ZHANG, F., ZHOU, Z., YANG, X. & HE, G. 2025 Knowledge-integrated additive learning for consistent near-wall modelling of turbulent flows. *J. Fluid Mech.* **1011**, R1.

ZHANG, T., CHEN, J., ZENG, F., TANG, D. & YAN, C. 2023 Improvement of transition prediction model in hypersonic boundary layer based on field inversion and machine learning framework. *Phys. Fluids* **35** (2).

ZHANG, X.-L., XIAO, H., LUO, X. & HE, G. 2022 Ensemble Kalman method for learning turbulence models from indirect observation data. *J. Fluid Mech.* **949**, A26.

ZHAO, Y., AKOLEKAR, H.D., WEATHERITT, J., MICHELASSI, V. & SANDBERG, R.D. 2020 RANS turbulence model development using CFD-driven machine learning. *J. Comp. Phys.* **411**, 109413.

ZHU, L., ZHANG, W., KOU, J. & LIU, Y. 2019 Machine learning methods for turbulence modeling in subsonic flows around airfoils. *Phys. Fluids* **31** (1).

DE ZORDO-BANLIAT, M., DERGHAM, G., MERLE, X. & CINNELLA, P. 2024 Space-dependent turbulence model aggregation using machine learning. *J. Comp. Phys.* **497**, 112628.